ELECTRONIC SUPPLEMENTARY INFORMATION (ESI)

Unveiling the high-temperature degradation mechanism of solid oxide electrolysis cells through direct imaging of nanoscale interfacial phenomena

Haneul Choi [a,b], Jisu Shin [a], Changho Yeon [c,d], Sun-Young Park[e], Shin-Tae Bae[f], Ji Wan Kim[f], Jong-Ho Lee [a,g], Jin-Woo Park [b], Chan-Woo Lee [c], Kyung Joong Yoon *[a] and Hye Jung Chang *[a,g]

[a]Center for Energy Materials Research, Korea Institute of Science and Technology, Seoul, 02792, Republic of Korea

[b]Department of Materials Science and Engineering, Yonsei University, Seoul, 03722, Republic of Korea

[c]Computational Science and Engineering Laboratory, Korea Institute of Energy Research, Daejeon 34129, Republic of Korea

[d]Department of Materials Science and Engineering, Korea University, Seoul 02841, Republic of Korea

[e]Technological Convergence Center, Korea Institute of Science and Technology, Seoul, Republic of Korea

[f]Green Energy Materials Research Team, Research & Development Division, Hyundai Motor Company, Uiwang-si, 16082, Republic of Korea

[g]Division of Nano Convergence, KIST school, University of Science and Technology, Seoul 02792, Republic of Korea

∗ Corresponding authors.
E-mail addresses: kjyoon@kist.re.kr (K.J. Yoon), almacore@kist.re.kr (H.J. Chang).
These authors contributed equally to this work.

This electronic supplementary information PDF file includes:

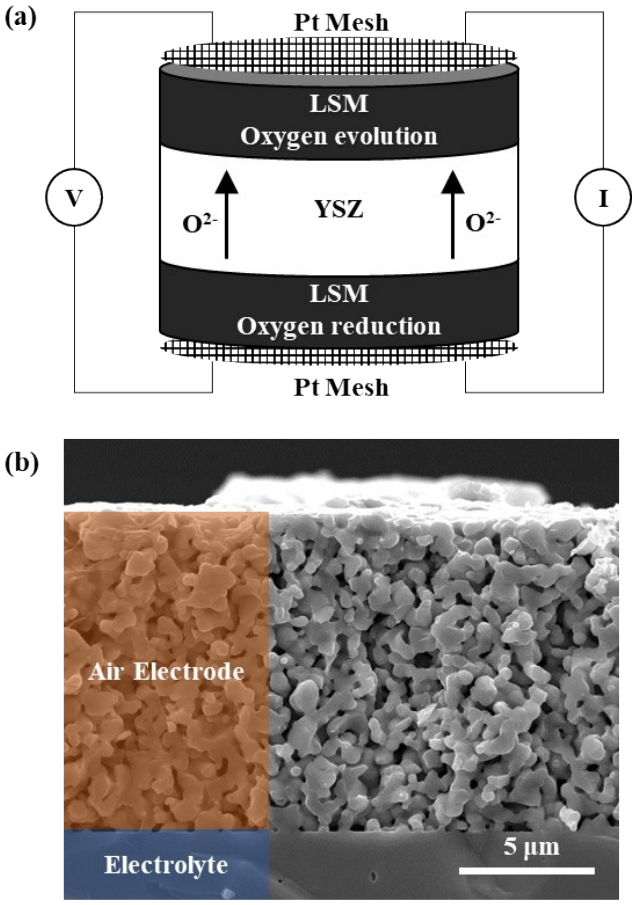

Fig. S1. Microstructure of the pristine cell. The electrochemical test was conducted using a symmetric cell, as illustrated in (a). The cross-sectional microstructure of the as-fabricated LSM air electrode deposited on the YSZ electrolyte was analyzed by SEM and TEM. (b) The secondary electron (SE) image shows a clean, unblemished interface.

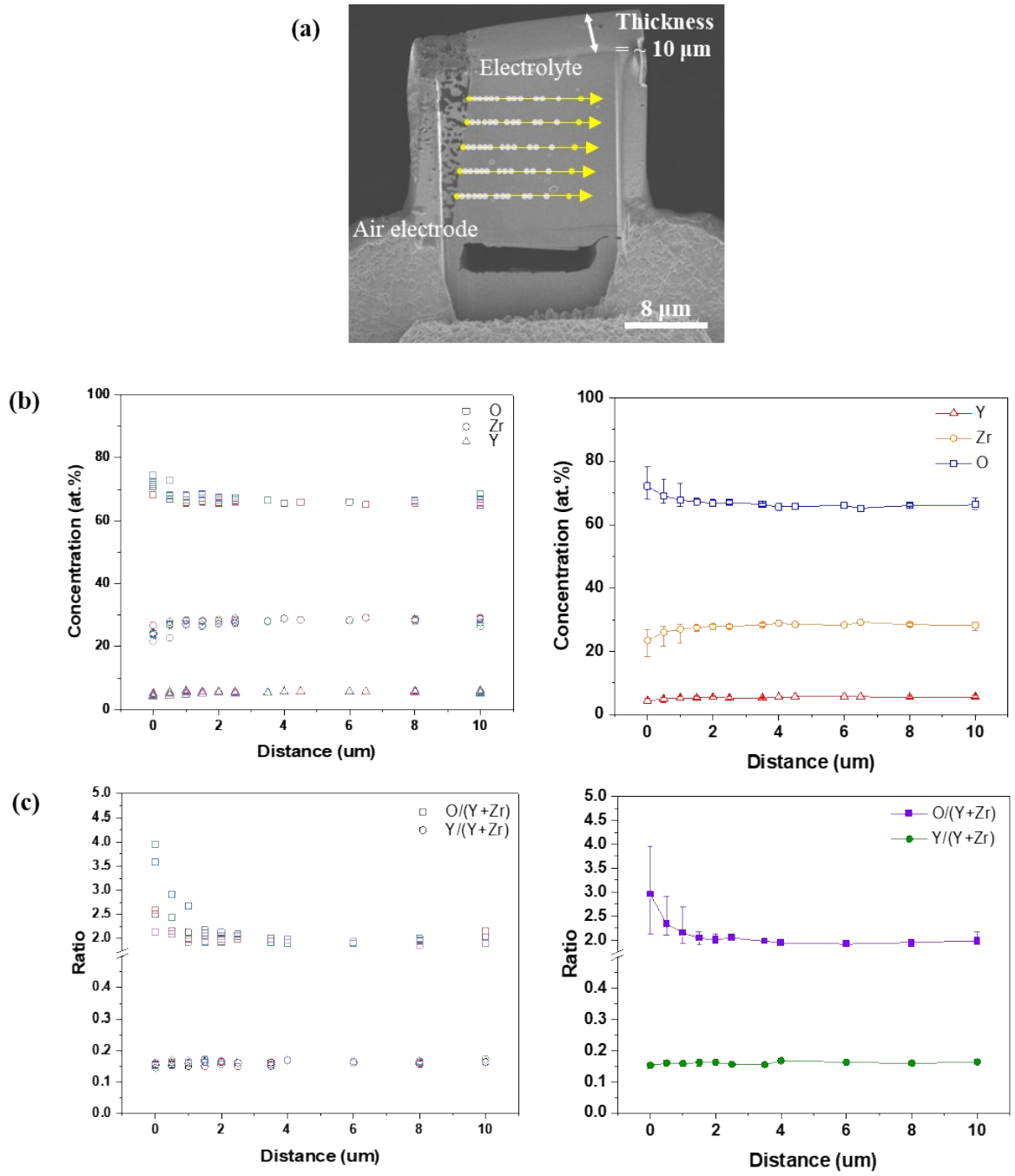

Fig. S2. (a) Backscattered electron (BSE) image of the specimen for EPMA analysis in operated cell. We prepared the specimen with a thickness of approximately 10 μm to perform EPMA analysis with a smaller interaction volume while maintaining sufficient signals using a FIB. In addition, a beryllium planchet was used to consider only the elements in the specimen. (b, c) Quantitative analyses were conducted through spot assessments along five distinct lines, as depicted in the BSE images. The error bars in concentration and ratio curve in Fig. 2(a) of the main text manuscript indicate the variability observed in these measurements.

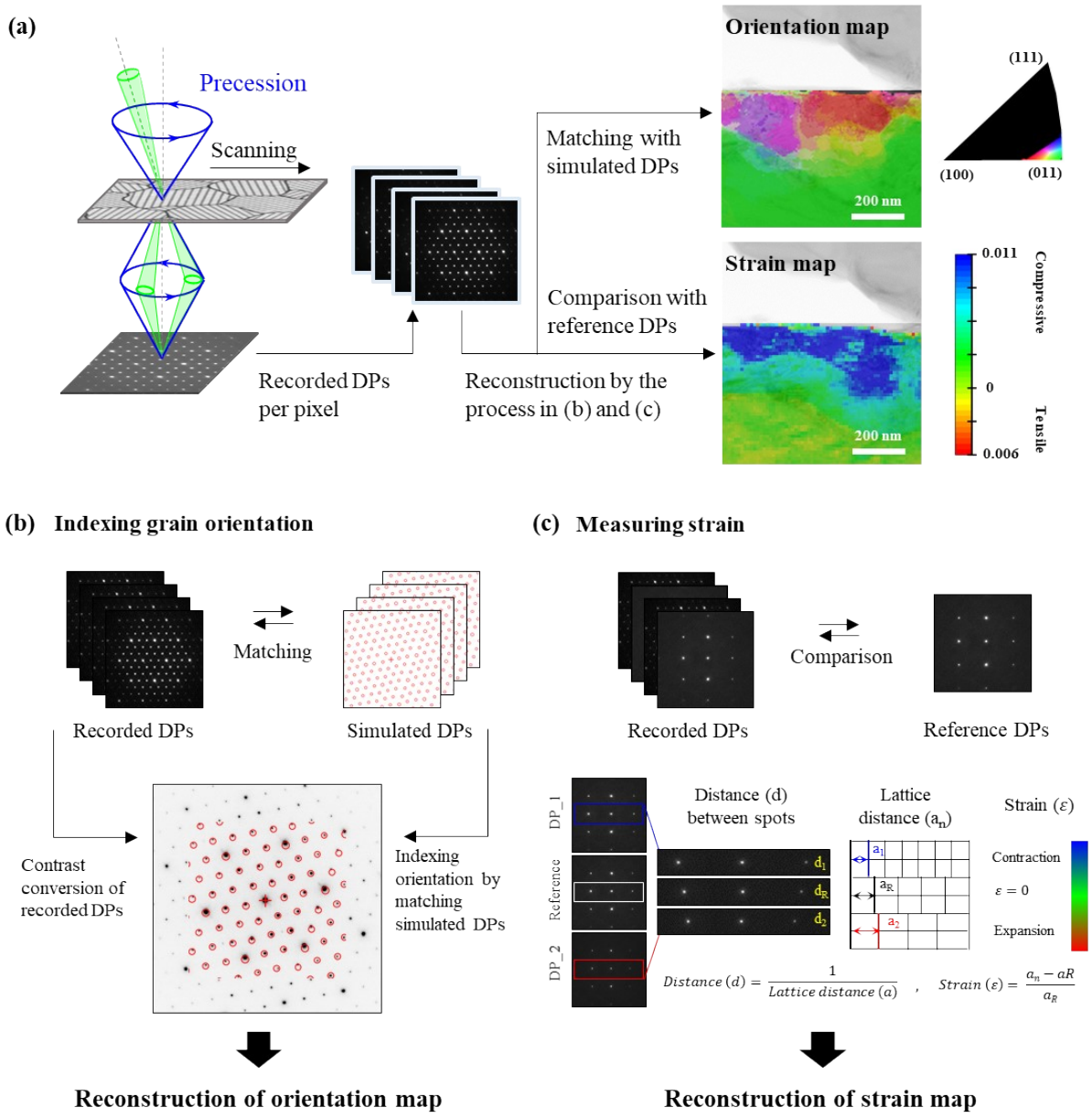

Fig. S3. Orientation and strain analysis using TEM with PED. Diffraction patterns (DPs) are recorded per pixel by scanning the specimen using PED. Recorded DPs can be reconstructed by two processes: (b) indexing the orientation by matching the simulated DPs, enabling the reconstruction of an orientation map, and (c) calculating the strain by comparing the lattice distance with that of reference DPs, enabling the reconstruction of a strain map.

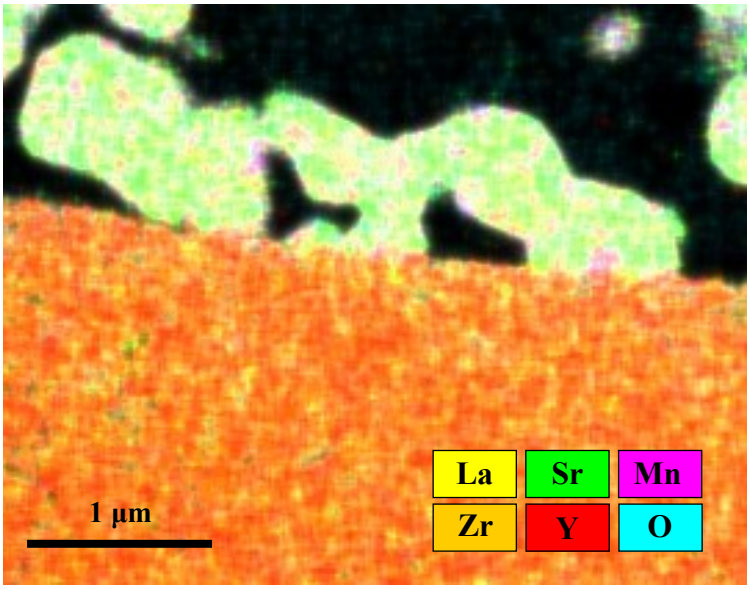

Fig. S4. Elemental distribution of the interface in the cell after operation. A TEM–EDS elemental map of the interfacial region confirming the homogeneous distributions of constituent elements of LSM and YSZ without significant chemical interactions or interdiffusion at the interface.

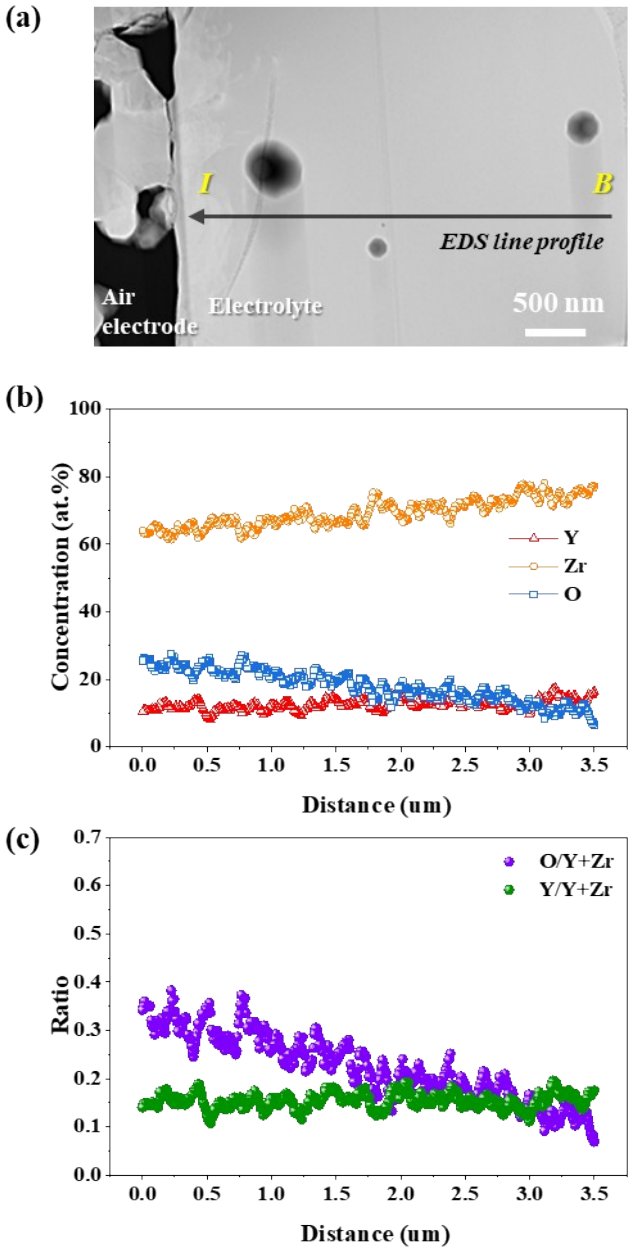

Fig. S5. STEM–EDS compositional analysis at the YSZ electrolyte in an operated cell. (a) HAADF–STEM image of the YSZ electrolyte in the interfacial region. EDS line analysis was performed along the arrow from the bulk region "B" to interface "I." (b) Concentration profile and (c) ratio of oxygen or yttrium relative to the sum of cations. The quantified values are somewhat different from the EPMA data in Fig. 2(a) and Table 1, as STEM–EDS can produce errors owing to the different absorption degrees of scattered characteristic X-rays for lightweight and massive elements. However, this analysis also shows an increase in oxygen from the bulk to the interface within a range of ~3.5 μm, which is consistent with the EPMA results.

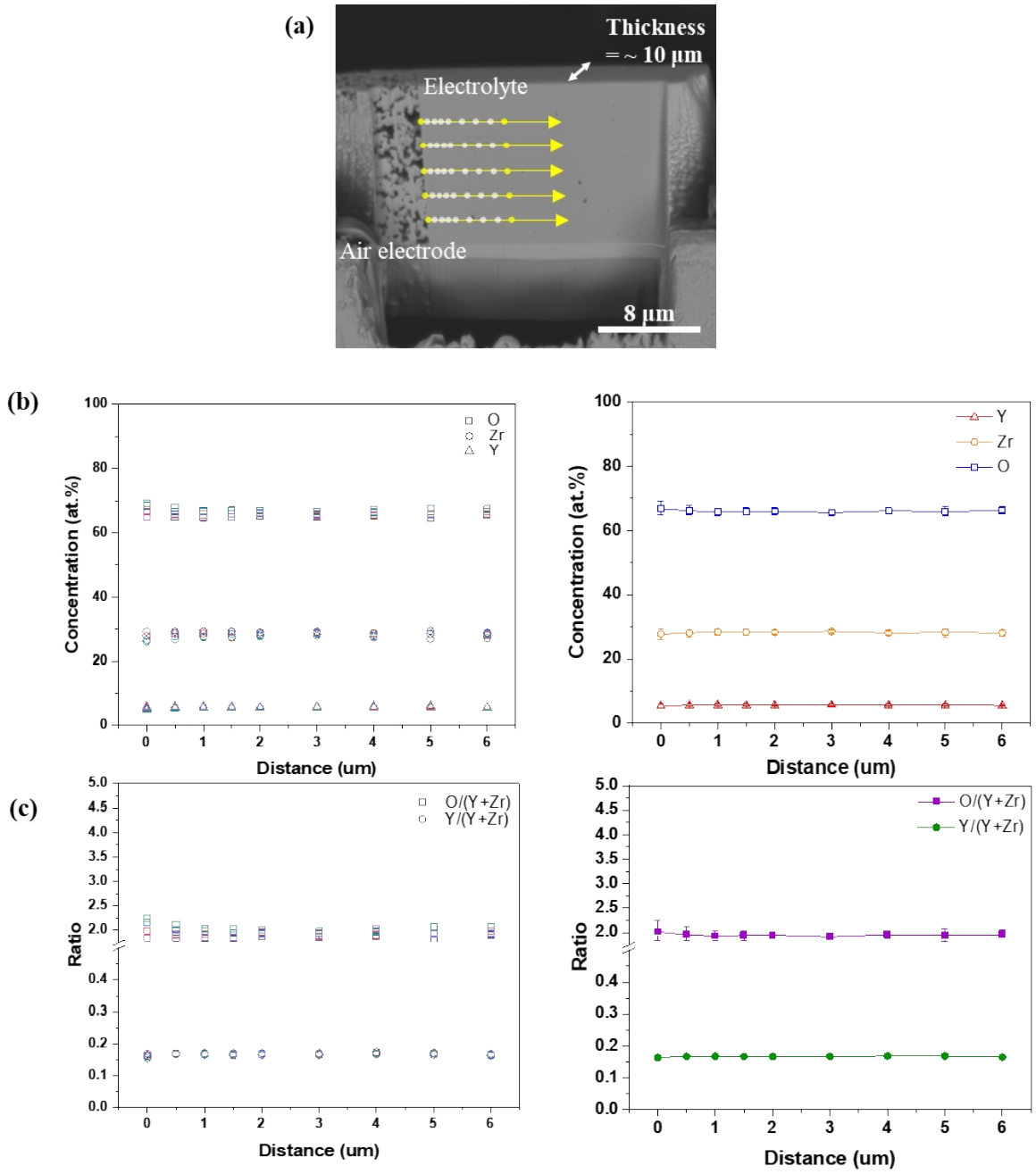

Fig. S6. (a) BSE image of the specimen for EPMA analysis in un-operated cell. (b, c) Quantitative analyses were conducted through spot assessments along five distinct lines, as depicted in the BSE images. The error bars in concentration and ratio curve indicate the variability observed in these measurements.

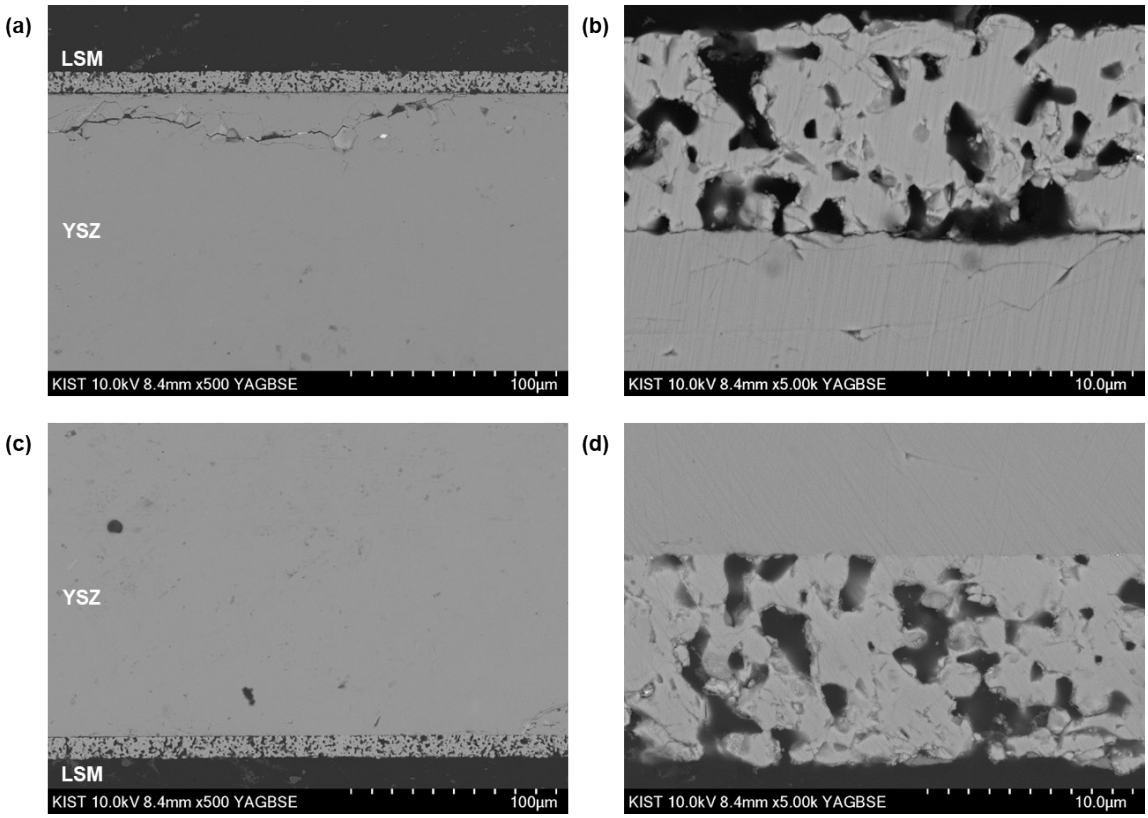

Fig. S7. BSE images of (a, b) anodically and (c, d) cathodically polarized electrodes in a symmetric cell operated at a current density of 3.6 A cm^{-2}.

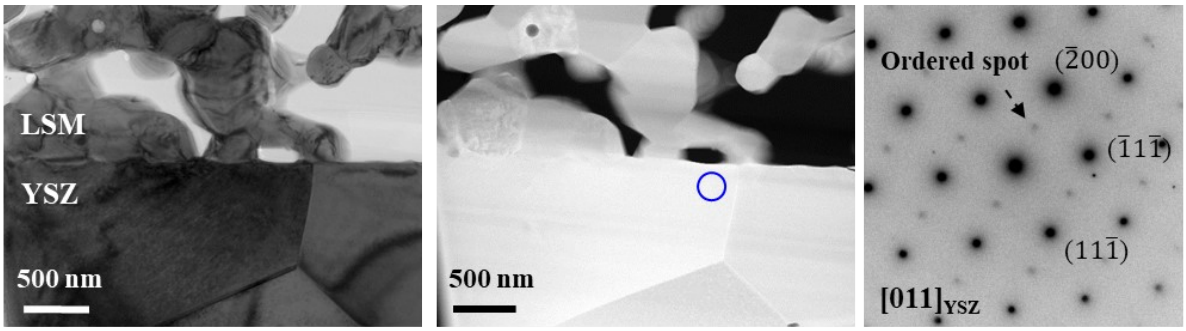

Fig. S8. The BF TEM image (left) and HAADF–STEM image (center) show a sound, defect-free interface between the electrode and the electrolyte in un-operated cell. The SADP (right) obtained from the blue circle in the HAADF–STEM image shows that before operation, the crystal structure of the 8 mol% YSZ has an ordered face-centered cubic structure.

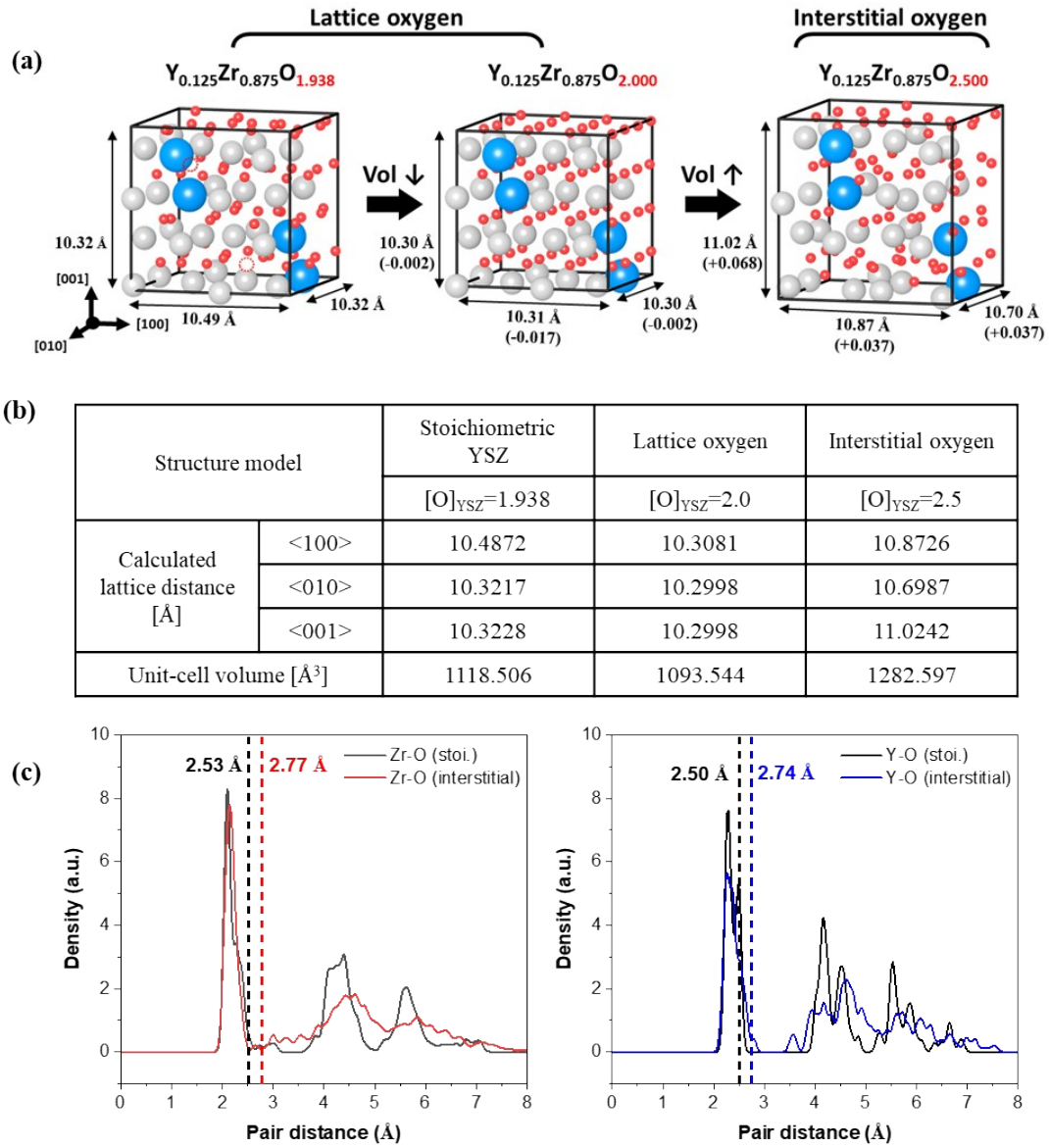

(b)

Structure model		Stoichiometric YSZ	Lattice oxygen	Interstitial oxygen
		$[O]_{YSZ}$=1.938	$[O]_{YSZ}$=2.0	$[O]_{YSZ}$=2.5
Calculated lattice distance [Å]	<100>	10.4872	10.3081	10.8726
	<010>	10.3217	10.2998	10.6987
	<001>	10.3228	10.2998	11.0242
Unit-cell volume [Å^3]		1118.506	1093.544	1282.597

Fig. S9. Consideration of lattice and interstitial oxygen in the DFT calculations. The unit-cell volume and lattice distances were estimated according to the accumulation of O^{2-} in two cases: lattice oxygen (left and center in (a)), wherein oxygen atoms are located at lattice oxygen sites, and interstitial oxygen (on the right in (a)), in which O^{2-} exists in the interstices of the unit cell. The lattice strain values in parentheses were calculated by comparing the lattice distance based on the stoichiometric YSZ model (left in (a)). (b) Lattice distances and calculated unit-cell volume of each YSZ model extracted from XRD simulations. (c) Weighted average lengths of cation–oxygen bonds calculated using the radial distribution function (RDF) of the stoichiometric YSZ (left) and the interstitial YSZ (right) when O^{2-} occupies interstitial sites. Each number indicates the weighted average of the Zr–O and Y–O bond length.

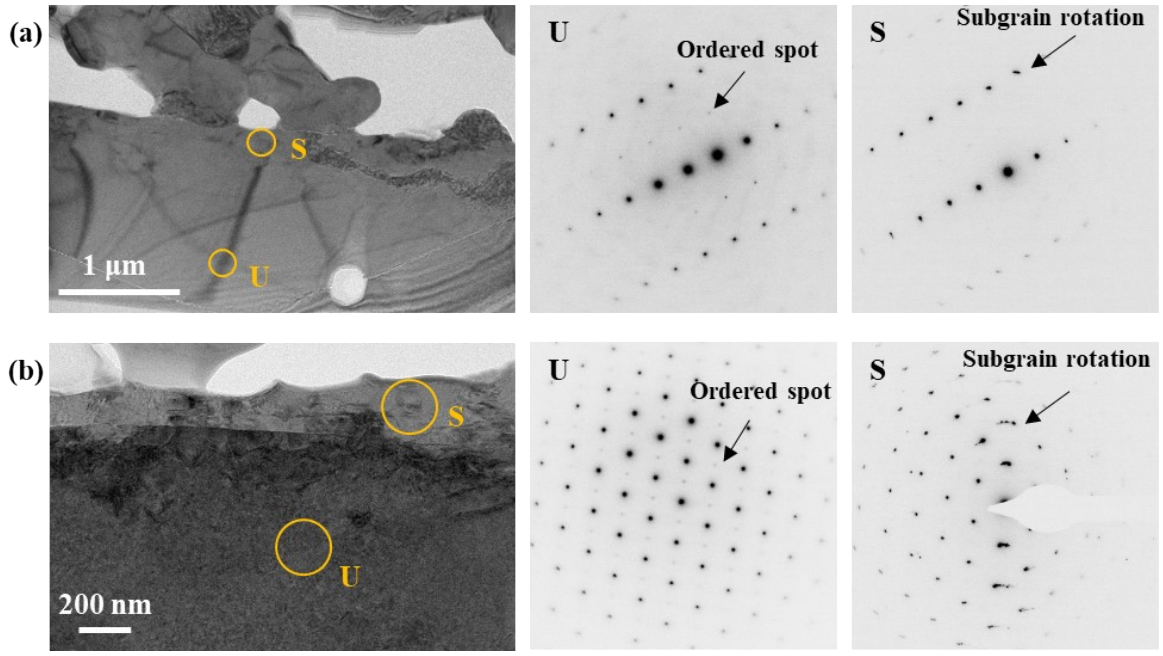

Fig. S10. Additional TEM images and corresponding SADPS showing the defect formation and order-disorder crystal structure transition of YSZ at the interfacial region. BF TEM images and corresponding SADPs showing changes in the interfacial crystal structure in other test specimens. SADPs (marked "U" and "S") were recorded from the bulk "U" and interface "S." The ordered spots in "U" disappeared in "S," which indicates an order–disorder transition at the YSZ interface. In addition, elongated spots appear at the interface "S," which reveal the formation of subgrains with low-angle boundaries.

(a) Before operation

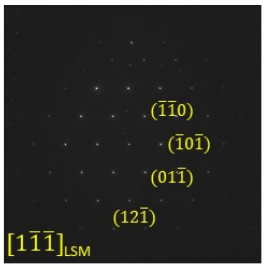

(hkl)	Measured lattice distance (d) [nm]	Calculated lattice parameter (a) [nm]	Average lattice parameter, a_0 [nm]
$(\bar{1}\bar{1}0)$	0.278396	0.393712	
$(\bar{1}0\bar{1})$	0.282008	0.398819	
$(01\bar{1})$	0.276817	0.391478	**= 0.393592**
$(12\bar{1})$	0.159363	0.390357	

$$\frac{a - a_0}{a_0} = 0.00603$$

(b) After operation

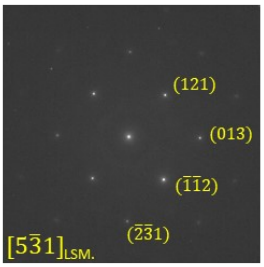

(hkl)	Measured lattice distance (d) [nm]	Calculated lattice parameter (a) [nm]	Average lattice parameter, a [nm]
(121)	0.161812	0.396358	
(013)	0.125313	0.396275	
$(\bar{1}\bar{1}2)$	0.16129	0.395079	**= 0.395966**
$(\bar{2}\bar{3}1)$	0.105876	0.396152	

Fig. S11. Estimated lattice parameters ($a_{avg.}$) of LSM (a) before and (b) after SOEC operation based on SADP.

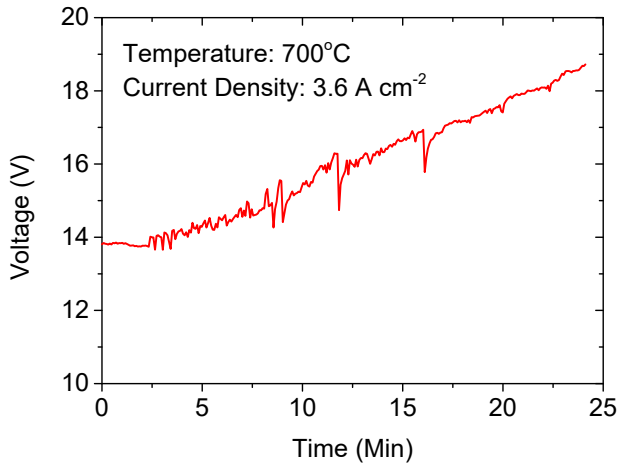

Fig. S12. Voltage of the cell operated at a higher current density of 3.6 A cm^{-2} at 700°C.

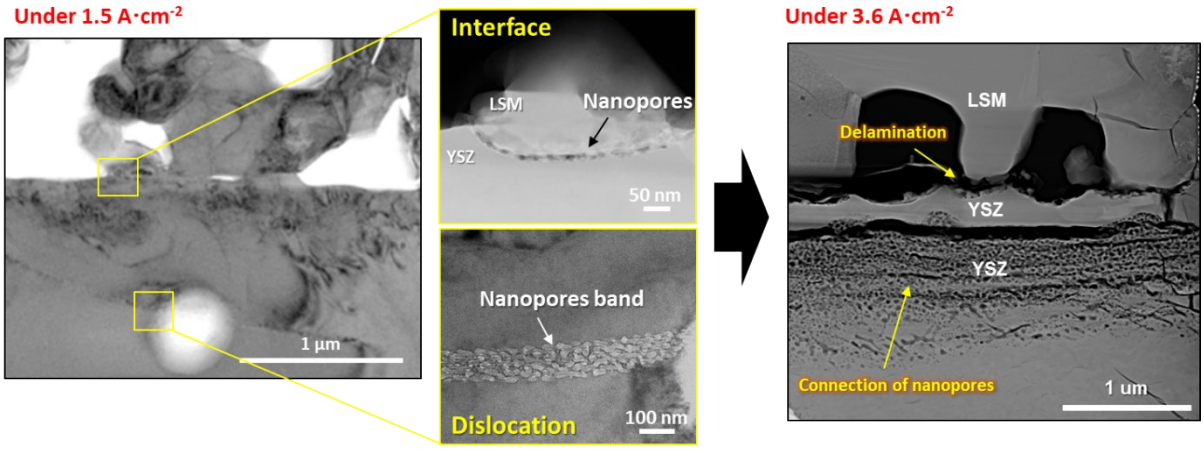

Fig. S13. TEM images of the cells operated at 1.5 and 3.6 A cm^{-2}.

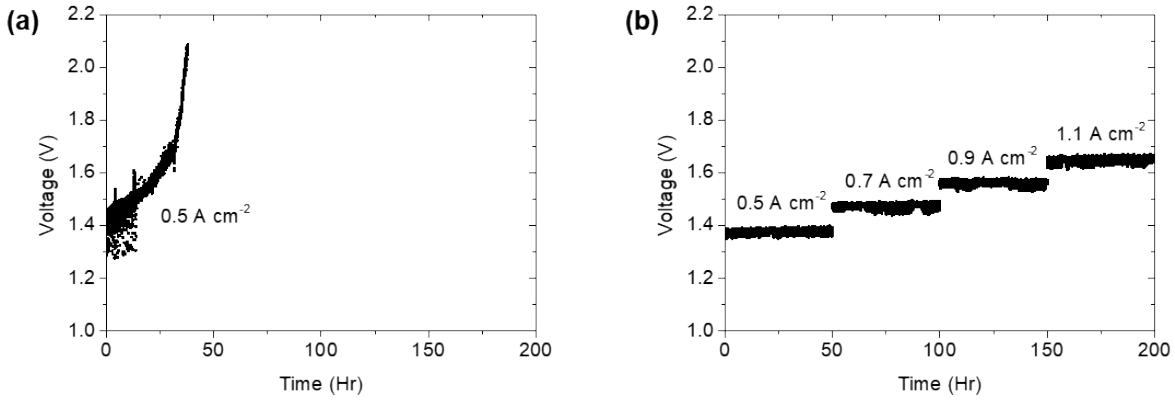

Fig. S14. Voltage of the electrolysis cells with (a) LSM air electrode at a current density of 0.5 A cm^{-2}, and (b) $La_2NiO_{4+\delta}$ air electrode with gradually increasing current density from 0.5 to 1.1 A cm^{-2} in increments of 0.2 A cm^{-2}.

Supplementary Note 1. Consideration of interstitial oxygen in DFT calculations.

Changes in the lattice distances caused by interstitial oxygen in YSZ were investigated using DFT calculations. The lattice distances and unit-cell volumes were extracted from the XRD simulation shown in Fig. S8(b). The non-stoichiometric model was constructed by adding oxygen atoms at interstitial sites in the stoichiometric YSZ model. The initial positions of interstitial oxygen were also uniformly distributed in the supercell to maximize the distance between oxygen vacancies. The lattice oxygen shown in Fig. S8(a) depicts oxygen-occupied oxygen vacancies, V_O, in the YSZ lattice, whereas the interstitial oxygen in Fig. S8(a) is oxygen occupying interstitial sites in YSZ after its oxygen lattice sites are filled at the oxygen composition ($[O]_{YSZ}$) of 2.0, as shown in the center of Fig. S8(a). Interestingly, opposite trends occur in the lattice volume between $[O]_{YSZ}$ =1.938 (left, Fig. S8(a)) → 2.0 (center, Fig. S8(a)) with compression and $[O]_{YSZ}$ = 2.0 (center, Fig. S8(a)) → 2.5 (right, Fig. S8(a)) with expansion, as shown in Fig. S8(b). The lattice expansion of $[O]_{YSZ}$ = 2.0→2.5 is due to additional oxygen ions occupying YSZ interstitial sites. As these are not lattice sites in the YSZ structure, YSZ inevitably expands its lattice to accommodate the extra oxygen ions. Such volume expansion occurs when interstitial oxygen ions, owing to their strong electronegativity, excessively capture electrons from neighboring cations within the crystal lattice, weakening the cation–oxygen bonds and increasing the bond lengths. In addition, the repulsion between oxygen ions in the model is maximized, so they strive to increase their distance from each other. Thus, in this study, which experimentally proves compressive strain, it is more appropriate to consider the accumulation of oxygen ions by substitution into oxygen vacancy sites within the YSZ lattice, rather than oxygen ions invading interstitially, thereby expanding the lattice. In addition, it can be concluded that the excess oxygen composition of $[O]_{2.592}$ measured in the EPMA analysis (Table 1 in manuscript), which is greater than $[O]_{2.000}$, is due to the oxygen ions that inherently exist at the numerous grain boundaries or dislocations at the LSM/YSZ interface.

Supplementary Note 2. Calculation of the weighted average bond length of interstitial oxygen using the radial distribution function (RDF).

In addition, the weighted average cation–oxygen bond length was calculated using the RDF when oxygen ions were occupying interstitial sites, as shown in Fig. S8(c). The plot confirms that the average Zr–O and Y–O distance distributions increased by 0.91Å. This is strong evidence for the above claims. Therefore, the excess oxygen composition of $[O]_{2.592}$ can be concluded to be due to the oxygen ions inherently present at the numerous grain boundaries at the LSM/YSZ interface.

Supplementary Note 3. Estimating the lattice parameter (a) using the selected area diffraction pattern (SADP)

Using the selected area diffraction pattern (SADP), the lattice parameter was estimated and calculated using Equation (1) below.

$$a = \sqrt{d_{hkl}^2(h^2 + k^2 + l^2)} \tag{1}$$

The calculated lattice parameters for LSM before and after SOEC operation are 0.0393592 nm and 0.0395966 nm, respectively (refer to Fig. S11). Relative to the LSM (before SOEC operation) lattice parameter, LSM after SOEC operation exhibited an approximate 0.603% expansion. This change in the lattice parameter of LSM was negligible compared to the severe alteration of the YSZ structure.

The lattice parameters for LSM before and after SOEC operation were calculated to be 0.0393592 and 0.0395966 nm, respectively (refer to Fig. S11). Relative to the lattice parameter of LSM before SOEC operation, that of LSM after SOEC operation expanded by approximately 0.603%. This change was negligible compared to the severe alteration in the YSZ structure.